

Estimation of the risk of airborne transmission in an elementary school classroom through Large Eddy Simulation

A. Vignolo*, M. Draper* and G. Usera*
Corresponding author: avignolo@fing.edu.uy

* Instituto de Mecánica de los Fluidos e Ingeniería Ambiental,
Facultad de Ingeniería, Universidad de la República, Uruguay.

Abstract: The pandemic of COVID-19 has had a major impact globally. Several authors have argued that the airborne transmission route of the virus SARS-CoV-2 plays a major role, particularly in poorly ventilated indoor environments. In this paper, the airflow inside a naturally ventilated elementary school classroom is simulated through highly resolved Large Eddy Simulation for a wintertime scenario. The flow results are qualitatively analyzed and the contagion risk is estimated through passive tracers, by coupling the simulation with the traditional Wells-Riley approach. Different window configurations and infected positions are considered. The developed numerical framework is able to capture the dynamics of the phenomenon, highlighting the importance of the spatial inhomogeneities.

Keywords: SARS-CoV-2, Airborne Transmission, Large Eddy Simulation, Wells-Riley, Natural Ventilation.

1 Introduction

By now the SARS-CoV-2 pandemic has caused the loss of millions of lives around the globe. Furthermore, in many cases health systems have been strained beyond their capabilities and the economical consequences have been notorious. The scientific community has therefore centered its efforts in understanding and reducing the transmission of the virus.

The transmission routes of SARS-CoV-2 have been a point of heated debate. The virus has been recognized from the start to be transmitted via droplets of fluid expelled by infected individuals during respiratory or vocalization events (e.g. breathing, coughing, sneezing, talking and singing). During quite some time the World Health Organization (WHO) only recognized the short-distance airborne transmission route, that is, that infection is caused by large expelled droplets, which follow ballistic trajectories and sink at a relatively short distance from the individual. Nonetheless, because of the insistence of the scientific community due to an increasingly large body of evidence, the long-distance airborne route was acknowledged as a possible way of transmission. This consists in smaller fluid droplets (some generated by evaporation), which can remain airborne and can be transported large distances by air currents. Thus, the ventilation of indoor environments and air disinfection has been put under the spotlight as a means of containing the pandemic.

One type of indoor environment in which attention has focused is primary schools. There have been several school closures in many countries, which has raised concerns about the adverse impact they could have on children. As classrooms usually hold stable populations during relatively large time intervals, many researchers have applied different variations of Wells-Riley risk models [1, 2, 3, 4, 5, 6]. Despite being useful models and although their simplicity is attractive, these models neglect spatial variations of transmission risk. In this context, Computational Fluid Dynamics (CFD) could provide a better understanding of airborne transmission, as it resolves the airflow inside the room [7].

Previous studies have applied CFD to resolve indoor airflows and to spatially assess infection risk. Nonetheless, many of them use a RANS (Reynolds-Averaged Navier-Stokes) approach. Concern has been raised that this technique might be ill-suited for resolving the indoors dispersion of airborne contaminants, as this process is mainly driven by turbulence, which is fully parametrized in the RANS approach [8]. Consequently, attention has been recently centered in Large Eddy Simulation (LES) for tackling this problem [8, 9]. LES resolves the largest turbulent scales, alas, it has a higher computational cost and requires much finer grids.

In this work we present a case study of a naturally ventilated primary school classroom in Montevideo, Uruguay, via a highly-resolved LES simulation. We spatially resolve the long-distance airborne contagion risk for SARS-CoV-2 by using passive scalar tracers (which have been shown to be a suitable surrogate for droplet nuclei for airborne transmission assessment [10]) and coupling results with a Wells-Riley approach, in a similar way to that of [8] and [9]. The main objective is to assess the importance of airflow patterns and inhomogeneities in risk assessment in the context of natural ventilation.

2 Methodology

2.1 Case description

The simulated classroom is a naturally ventilated room with a surface area of $6\text{ m} \times 8\text{ m}$ and a height of 3.5 m . It has four double casement windows facing west, which communicate directly to the school playground. On the opposite wall, facing east, there is a door and an awning window, which communicate with a central corridor. Figure 1 depicts the west and east walls and the position and dimensions of the room openings.

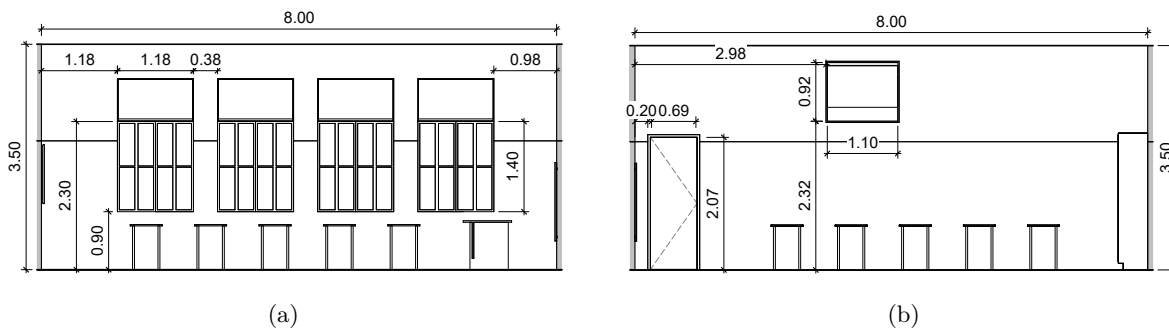


Figure 1: Studied classroom. (a) shows the west wall and (b) shows the east wall. All dimensions are in m.

The classroom holds a population of 30 children and a teacher. Two children sit per table, generating a quincunx pattern, as shown in Figure 2. This was one of the sitting patterns used during the pandemic in the studied classroom.

2.2 Numerical CFD framework and modelling

2.2.1 Flow solver

Computations were carried out using CHAMAN (*Computación Heterogénea en Mecánica*), an in-house, open-source, general purpose CFD software [11, 12]. This software stems from the *caffa3d.MBRi* code [13, 14] by adding the capability of Heterogenous Computing (using both CPUs and GPUs).

As well as its predecessor, CHAMAN is a finite volume, incompressible flow solver, which is second-order accurate in both space and time. It uses collocated orthogonal grids (or, alternatively, curvilinear body-fitted grids) distributed in unstructured blocks, each one containing a structured grid, which are grouped in unstructured computing regions. Computation among regions is parallelized via the MPI (Message Passing Interface) library.

CHAMAN solves a mathematical model which comprises the incompressible mass balance equation (1), the momentum balance equation for a viscous and incompressible fluid (2) and a passive scalar transport equation (3):

$$\int_S (\vec{v} \cdot \hat{n}_S) dS = 0 \quad (1)$$

$$\int_{\Omega} \rho \frac{\partial \vec{v}}{\partial t} d\Omega + \int_S \rho \vec{v} (\vec{v} \cdot \hat{n}_S) dS = \int_{\Omega} -\rho \beta (T - T_{\text{ref}}) \vec{g} d\Omega + \int_S -p \hat{n}_S dS + \int_S 2\mu D \cdot \hat{n}_S dS \quad (2)$$

$$\int_{\Omega} \rho \frac{\partial \phi}{\partial t} d\Omega + \int_S \rho \phi (\vec{v} \cdot \hat{n}_S) dS = \int_S \Gamma (\nabla \phi \cdot \hat{n}_S) dS + \int_{\Omega} q_{\phi} d\Omega \quad (3)$$

where Ω is a control volume delimited by a surface S with a unitary normal vector \hat{n}_S (outwards pointing), \vec{v} is the fluid's velocity, ρ is the density, β is the coefficient of thermal expansion, T is the fluid's temperature, T_{ref} is the reference temperature for β , \vec{g} is the gravity field, p is the pressure, μ is the fluid's dynamic viscosity, D is the strain tensor, ϕ is a scalar field and Γ is its associated diffusivity. Finally, q_{ϕ} represents the tracer's volumetric generation rate. It should be noted that the coupling of thermal effects is modelled via the Boussinesq approximation. Furthermore, equation (3) is used to represent both the energy balance (by setting ϕ to T and Γ to $k/c_p = \mu/Pr$) and to represent the transport of other passive scalars, such as airborne contaminants, in an Eulerian phase.

The mathematical model is expressed in the Cartesian coordinates of the grid, linearized and iteratively solved at each time step by employing an outer-inner iteration scheme and either SIP or AMG solving algorithms. The SIMPLE method for pressure-velocity coupling is used [14]. Several implicit time-stepping methods can be used, in this work we have selected a three time level scheme.

Finally, regarding subgrid modelling, the standard Smagorinsky model was used [15].

Further information regarding CHAMAN and `caffa3d.MBRi`, as well as detailed application examples, can be found in [12, 13, 14, 16, 17]

2.2.2 Case settings

For the simulation at hand, the domain was divided into 30 parallelized computation regions, each consisting of a uniform Cartesian grid with 9.145.000 cells, which totalizes 274.352.400 domain cells. The achieved resolutions in the x , y and z directions (defined as shown in Figure 1) are 8.4 mm, 7.9 mm and 9.2 mm, respectively. This is quite high for usual simulations in the context of indoor airflows, particularly considering the dimensions of the domain [18, 19, 20]. It should also be noted that many studies use RANS simulations, which require less resolution. The highest resolution for a similar LES problem is, to the best of our knowledge, the one presented in [8] (9.24 mm \times 9.24 mm \times 9.69 mm).

Simulations were run using a four spot virtual machines setup in GoogleCloud Compute Engine, comprising a total of 32 GPUs Nvidia K80, with 12 GB RAM each, for a total of 384 GB RAM.

Furthermore, a time step of 0.1 s has been used, which, for the boundary conditions specified further ahead, leads to a Courant number just above 2. This is deemed acceptable based on previous experience and the fact that CHAMAN is mainly an implicit CFD solver.

Individuals and some furniture were represented within the domain by using the Immersed Boundary Method (IBM) [21]. STL files for the teacher and the students were obtained from [22] and students desks were modelled in Autodesk Inventor and exported to STL format. A unified patch containing information for all objects was preprocessed before running the simulation. Figure 2 depicts the resulting arrangement. It is worth noticing that the IBM gives CHAMAN great flexibility for representing complex geometries while keeping meshing relatively simple.

Boundary conditions were imposed as follows, with the aim of representing a cross-ventilation scenario. A uniform speed boundary condition of 0.182 m/s was prescribed at one of the exterior windows in order to set a ventilation rate of 6.4 ACH (Air Renovations per Hour). This value was selected in accordance to WHO's recommendation for the pandemic [23]¹. The inflow temperature was set to 14 °C. The other (closed)

¹Although this ventilation rate, which is well above ASHRAE's 62.1 standard [24] minimum requirement for schools (3.8 ACH for this room), might seem rather high, a measurement campaign (not reported here) allowed to infer that similar window configurations could provide even higher ventilation rates.

windows were set to a wall boundary condition with $15\text{ }^{\circ}\text{C}$. Two different scenarios were simulated, one with the open window at the back of the room and the other one with the open window at the front. The room walls, ceiling and floor were also set as non-slip boundaries with a uniform temperature of $18\text{ }^{\circ}\text{C}$. These temperatures are feasible for the Uruguayan winter. Additionally, outlet (null gradient) boundary conditions were set at the interior awning window and at the door. Finally, both the teacher and the students immersed boundaries had a prescribed body temperature (below the neck) of $28\text{ }^{\circ}\text{C}$ and a head temperature of $33\text{ }^{\circ}\text{C}$. These values were selected in accordance to the configurations reported in [8] and [9]. Immersed boundary temperatures were prescribed by introducing a heat source within each patch cell. Said source is modulated for each cell proportionally to the difference with the target temperature, and is updated at each time step. This technique was observed to be stable.

Furthermore, two passive scalar tracers were considered, both of which were used to represent an airborne pathogen emission and dispersion from two possibly infected individuals. All tracer sources were defined as spheres with a diameter of 10 cm, with their centers set 15 cm in front of the mouth. This aims at representing an already dispersed pathogen exhalation [8]. Momentum associated with inspiration and exhalation is neglected. The net tracer generation is equally divided among all the cells within the sources. Figure 2 shows the tracer sources in front of each infected individual. The emission rate set will be addressed in section 2.3.4.

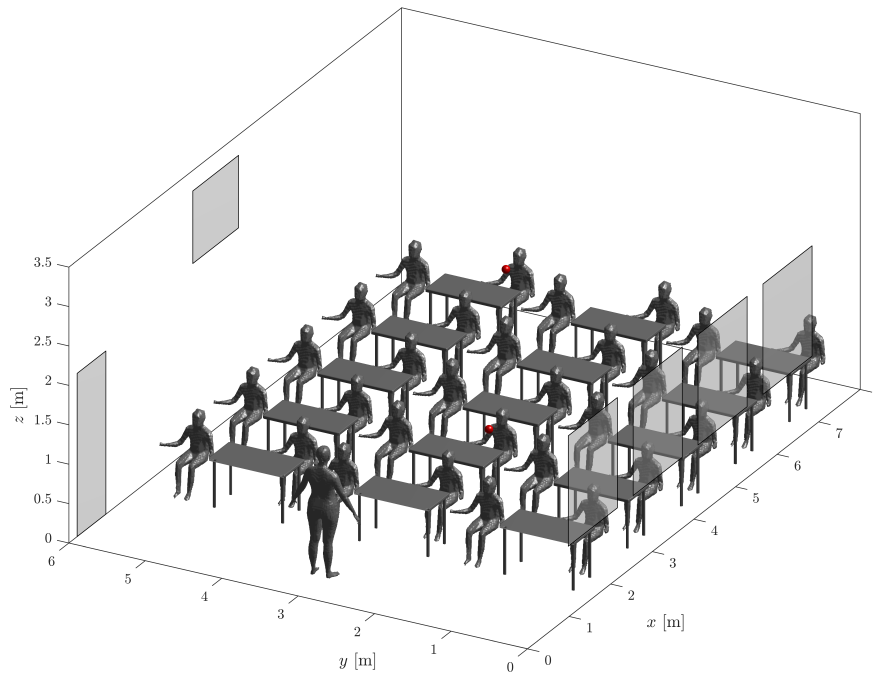


Figure 2: Immersed Boundary Conditions for the classroom domain, representing 30 children, 15 desks and the teacher. The room windows and door are depicted by grey rectangles and the tracer sources are represented by red spheres in front of the infected individuals.

It is interesting to notice that as passive tracers do not alter the flow, different tracer fields can be used to independently simulate the dispersion of pathogen from different locations (i.e. selecting different positions for the infected individuals) in the same CFD simulation, which considerably reduces the computational load. Furthermore, as the tracer transport equation is linear in the tracer field, it follows that tracer emission can be scaled as wanted, and therefore individual simulation of different emission rates is unnecessary. Finally, the tracer fields associated with different sources can be added to obtain the cumulative pathogen concentration for the cases where more than one infected individual is present.

Initial conditions for velocity and tracer concentrations were set to zero and a uniform temperature of $18\text{ }^{\circ}\text{C}$ was prescribed. These conditions aim at roughly representing an initially empty classroom with closed windows. The simulation was run for one physical hour, which required approximately 10 computation days.

Mean fields were observed to have reached steady state at that point. The problem was then run for an additional half hour in order to compute mean fields.

2.3 Risk assessment methodology

2.3.1 Wells-Riley models

The risk assessment methodology employed is based upon Wells' hypothesis and his concept of quanta [25]. Wells devised the latter as a certain amount of a pathogen which can, on average, cause the infection of an individual. Wells' hypothesis expresses that the probability of infection of an individual within a room via the long-distance airborne route can be modelled with a Poisson distribution. It is proposed that the distribution's parameter, λ , corresponds to the total amount of quanta inhaled by the individual after a certain time. It follows that the probability of infection of at least one person, P , can be expressed as shown in equation (4).

$$P = 1 - e^{-\lambda} \quad (4)$$

Several ways of estimating λ have been proposed, resulting in the Wells-Riley models family². Different approaches have allowed to represent additional physical processes (e.g. virus inactivation and filtration) and to relax certain hypothesis (e.g. Riley's model required steady-state conditions). Nowadays almost all applications of the Wells-Riley models stem from either the Gammaitoni-Nucci [27, 28] or the Rudnick-Milton [29] methods, both of which have found widespread use in the context of the SARS-CoV-2 pandemic [1, 2, 3].

2.3.2 Coupling of Wells' hypothesis with CFD

Despite their undeniable usefulness, traditional Wells-Riley models have certain limitations. In particular, they rely on the perfect-mix hypothesis: they assume that the pathogen is homogeneously and instantly distributed in the room (i.e. they are box models). Therefore, spatial quanta and risk variations are neglected. Concern has been raised that this could underestimate the risk of infection [9]. CFD has been proposed as a suitable tool for evaluating this issue, and several works have introduced ways of coupling it with Wells-Riley methods [8, 9, 30].

For this paper, we have coupled the Wells-Riley approach with the CFD method as follows. The total number of quanta inhaled by an individual can be calculated as given in equation (5):

$$\lambda = p \int_0^T C(t) dt \quad (5)$$

where C is the tracer (quanta) volumetric concentration in the inhaled air, T is the total time elapsed since the considered event begun (i.e. class time elapsed) and p is the mean pulmonary ventilation rate, which we assume to have a constant value of 800 L/h, according to what is reported in [31] for a breathing (not talking) person. It should be noticed that the spatial dependency of risk is implied in the value of C . To approximate this concentration, we suppose children inhale air from a cubic volume centered on the horizontal plane at their nose level. We assume that school children breath 20 times per minute [32] which, for the selected value of p , implies a volume of 667 cm³ per breath, and therefore a cube of side 8.74 cm. Consequently, we build an airborne contagion risk map by solving equation (5) for each simulation grid cell at nose level using the spatial concentration average over the described cube centered at the cell at hand. The time integral is approximated by a finite sum, resulting in equation (6):

$$\lambda = p \sum_i \tilde{C}_i \Delta t \quad (6)$$

where the index i covers the simulation time steps and the tilde denotes the spatial average. It should be noted that the latter is a tridimensional moving mean operation. The calculated value of λ is then plugged in equation (4) for estimating the risk of infection.

²Named after the work of Riley and his collaborators [26].

2.3.3 The Gammaitoni-Nucci model

We have selected the Gammaitoni-Nucci model [27, 28] for comparison with the CFD coupled results, as it allows for a transient quanta concentration in the system. Furthermore, it incorporates the ventilation rate as an explicit parameter, which is known for the case of study.

The quanta inhaled by an individual is estimated by performing a mass balance to the considered room under the perfect mix hypothesis. Assuming that the air entering the room is pathogen-free, the mass balance can be written as

$$\frac{dN(t)}{dt} = qI - \frac{Q}{V}N(t) \quad (7)$$

where N is the number of quanta in the room, V is the room's volume, t is the time and Q is the volumetric airflow entering and leaving the room. qI expresses the generation of quanta within the room as the product of the number of infected individuals I and the quanta generation rate per person q , which is supposed to be the same for each infected individual. Equation (7) does not consider quanta sinks such as disinfection UV lights, pathogen deposition and inactivation, but those processes can be easily modeled by summing additional pathogen elimination rates to Q [33].

Equation (7) can be integrated to obtain the N . Then, the amount of quanta inhaled by an individual over a certain time period T can be expressed as

$$\lambda = \frac{pIq}{Q} \left[T + \left(\frac{N_o}{Iq} - \frac{V}{Q} \right) \left(1 - e^{-\frac{qT}{V}} \right) \right] \quad (8)$$

where N_o is an initial condition for quanta, which is herein assumed to equal zero. We will also assume $I = 1$ (only one infected at a time), as it is usually done for risk assessment via Wells-Riley models.

2.3.4 Quanta emission rate

The main difficulty for applying Wells-Riley models to real scenarios is determining the appropriate quanta emission rate for an infected individual. This parameter, which depends on the pathogen considered and how contagious it is via the long distance airborne route, has been traditionally backwards-calculated by fitting epidemiological data [33]. Nonetheless, given the difficulty of this approach and the lack of available data for SARS-CoV-2, recently Buonanno, Stabile and Morawska [34, 35] have proposed a novel method for estimating the quanta emission rate by measuring the viral load in the saliva of infected individuals. Although high uncertainties prevail, this method has allowed for determination of a probability density function for the quanta emission rate [34]. Moreover, it has been possible to associate certain quanta emission rate values to certain respiratory events (breathing, talking, coughing, singing, etc.).

For example, based in Buonanno's results, in [3] quanta emission rates of 1 quanta/h and 5 quanta/h are given for SARS-CoV-2 as representative values for quiet and noisy classrooms, respectively. Nonetheless, this assessment was done prior to the appearance of newer and more contagious SARS-CoV-2 strands, such as Delta and Omicron [36]. Therefore, some researchers have decided to use much higher values in recent studies, of up to 100 quanta/h [8]. Great variation is therefore possible.

For the present paper we have selected a quanta emission rate of 1 quanta/h. Although this value corresponds to the mentioned recommendation for a quiet classroom, we have principally chosen it in order to generate scalable results. The total number of quanta inhaled by an individual is proportional to the quanta emission rate, both via the CFD approach³ and the Gammaitoni-Nucci equation⁴. Furthermore, for small values of λ , equation (4) can be linearized around $\lambda = 0$ without introducing important errors. Therefore, the infection risk is approximately proportional to the quanta emission rate. Consequently, the risk maps presented in section 3.2 and the results obtained via the Gammaitoni-Nucci model can be scaled to fit any pathogen by simply multiplying the reported risk by the appropriate quanta emission rate, expressed in quanta/h. We will therefore focus the analysis on discussing the spatial risk distribution without dwelling too much on the actual absolute risk value.

It should be noted that for very big values of λ , the linearization of equation (4) could introduce large errors. Nonetheless, we have observed that for the parameters of the case of study, the relative error remains

³Due to the linearity of equation (3) in ϕ , see section 2.2.2.

⁴This strictly only occurs for $N_o = 0$, as is considered in the present study.

bellow 1% for a quanta emission rate of 100 quanta/h when estimating λ from equation (8), which is deemed acceptable, as it is probably well below the uncertainty of q estimations.

3 Results and discussion

3.1 Qualitative description of the flow

For both simulation cases, the flow was observed to be quite complex. Thus, we first focus on performing a qualitative description of the flow and its main features by examining orthogonal slices of different fields.

The flow was observed to have reached a statistical steady state by the end of the first simulation hour for both cases. Therefore, mean field values were obtained by averaging over a 30 minute window after the first simulation hour.

3.1.1 Case 1: rear window open

For the first case, in which the inflow boundary condition was set at the back of the classroom, the results shown in Figures 3, 4, 5 and 6 were obtained.

The velocity field components in Figure 3 show how the air entering the room (with only a positive y velocity component) quickly sinks due to buoyancy (negative z velocity component), as it is colder than the air inside. The inflow draft then impacts the floor, spreads radially from the impact point and continues moving just above the floor, forming a cold low draft. It should be noticed that this draft exhibits a contraction with respect to the inflow area, and therefore increases its speed with respect to the inflow condition just after reaching the floor.

Figure 4(a) shows how part of the cold draft moves along the y axis (positive y velocity component), impacts on the wall at $y = 6$ m and is then redirected towards the door (negative x velocity component). Another part reaches the front of the classroom and is then redirected towards the door. Finally, a diagonally-moving draft reaches the door with no turns. While thermal plumes start forming from the feet of the occupants, these are rather small and do not significantly alter the flow, which is essentially bidimensional.

On the middle height levels of the room, airflow becomes more complex, and many recirculations arise, as can be appreciated in Figure 4. Most noticeably, at the children's mouth level, recirculations mainly redirect the air towards the side of the inflow boundary condition and the front of the room, where the teacher stands, is quite stagnant. The dynamic on these middle levels is less directly influenced by the inflow boundary condition, and horizontal velocity components are of lower magnitude. In turn, the vertical velocity component becomes preponderant, as thermal plumes dominate the air movement near the room occupants. Air rises within the plumes and ultimately reaches the ceiling, where it spreads horizontally and descends near the walls and in-between plumes while reducing its temperature. This effect is most notorious next to the closed windows, where localized downwards drafts are stronger, as the closed window panes are colder than the walls. Therefore, a tridimensional airflow is developed, with notorious vertical mass advection.

The room's temperature field, depicted in Figure 5, attests to the described airflow. There is a clear division between the lower portion of the room (i.e. mouth level and below), where the temperature is around 1 °C above the inflow boundary condition, and the upper portion, where the temperature is higher due to the heating induced by the teacher and students. After an hour, the latter reaches almost 19 °C, 1 °C above the initial and wall boundary conditions. Both zones have a rather homogeneous temperature field.

Finally, Figure 6 explores the pathogen (i.e. passive tracer) distribution for both the infected student at the front and at the back of the classroom. The tracer distribution provides a complementary depiction of how the airflow evolves inside the classroom. In the case of the student at the front of the class, the emitted tracer is both horizontally and vertically transported. The horizontal advection is mainly towards the open window, to the back and left of the infected student, as a consequence of the previously observed recirculation at the students' mouth level. The vertical advection is caused by the thermal plumes. The tracer reaches the ceiling next to the inflow wall and is mainly transported to the front of the class, descending to lower heights due to the downwards flow at the closed windows and at the walls, and also in-between thermal plumes.

On the other hand, in the case with an infected child sitting at the back, there is a higher tracer dispersion all over the classroom, particularly at breathing level, although higher concentrations are attained at the back. Again, the tracer field evidences considerable vertical mass advection, induced by the thermal plumes.

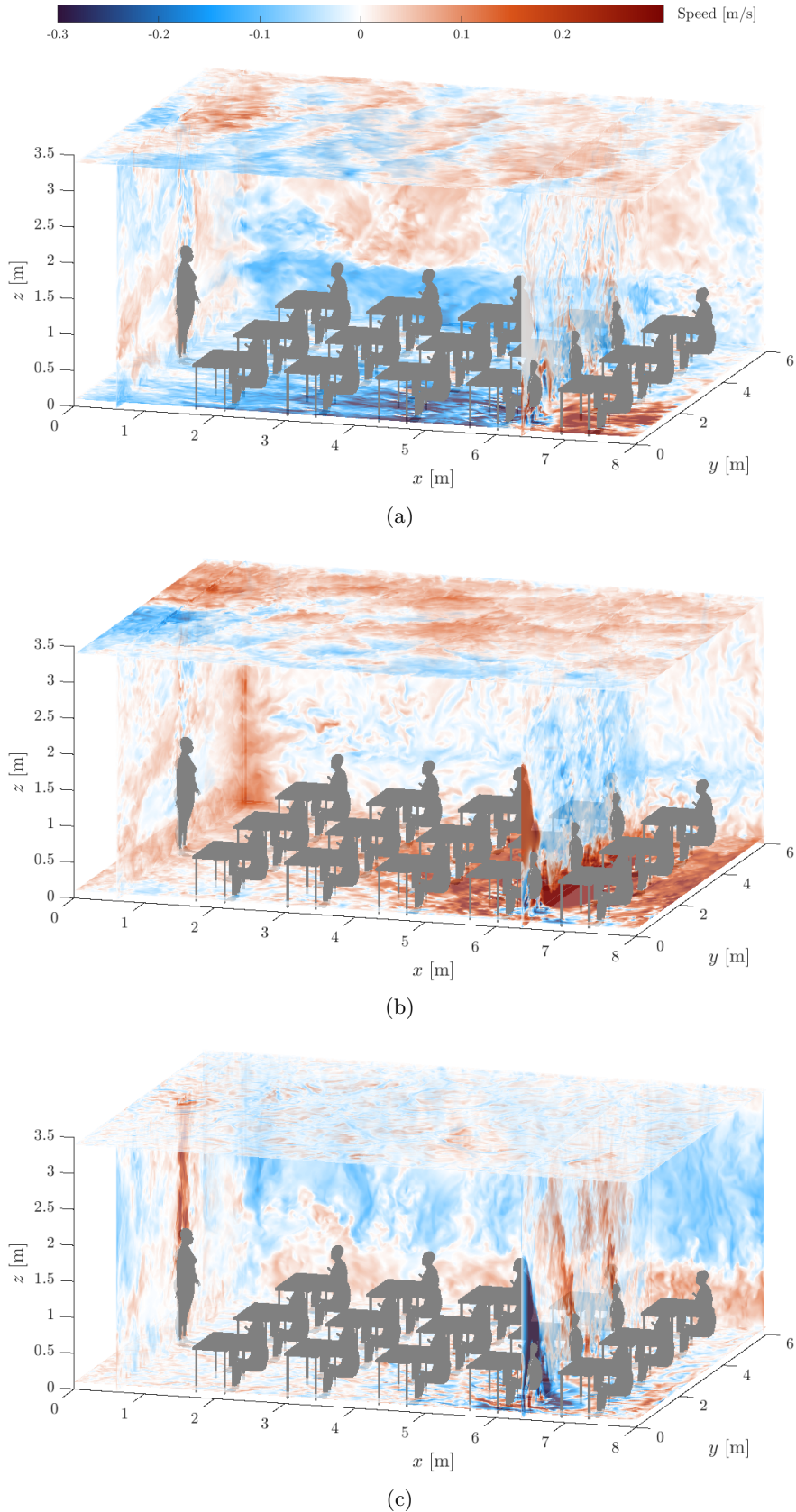
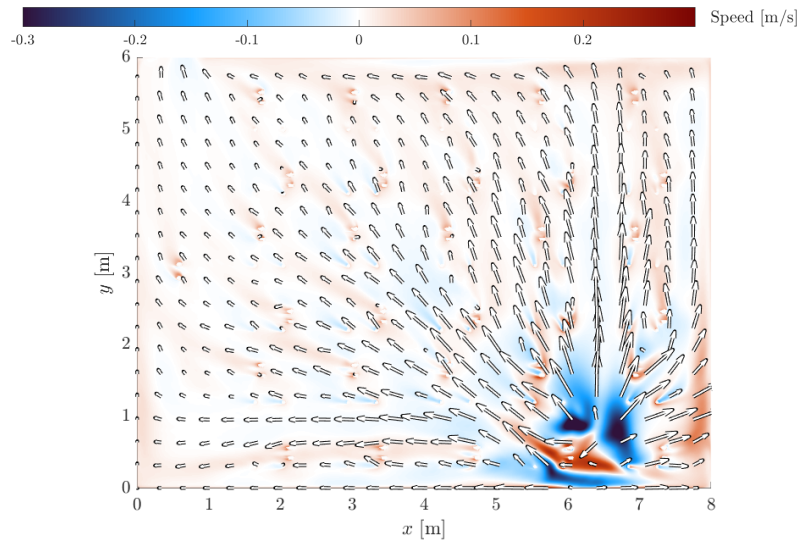
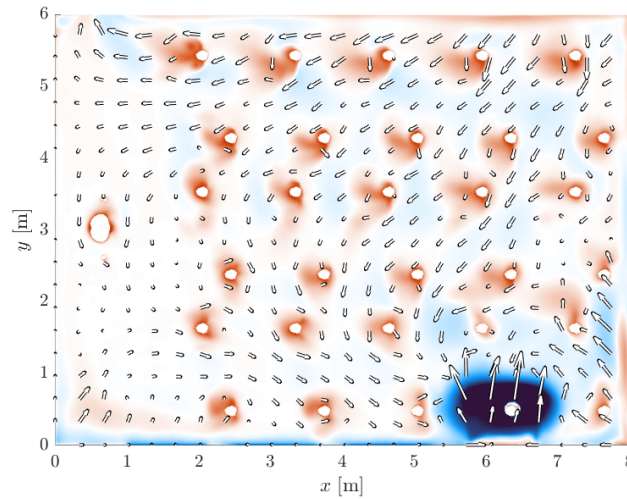


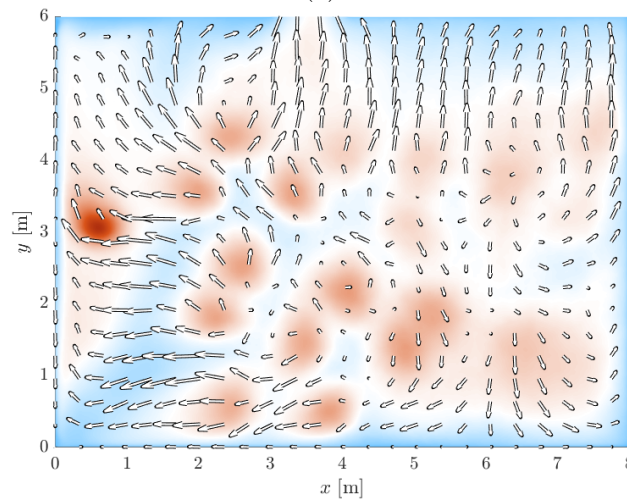
Figure 3: Velocity field slices for case 1. (a), (b) and (c) show the instantaneous velocity x , y and z components, respectively, after an hour of simulation.



(a)



(b)



(c)

Figure 4: Mean velocity field at different horizontal planes for case 1: (a) at 10 cm from the floor, (b) at the children's mouth level and (c) at the middle of the awning window. The coloured background corresponds to the vertical velocity component and the arrows show the horizontal projection of the velocity field.

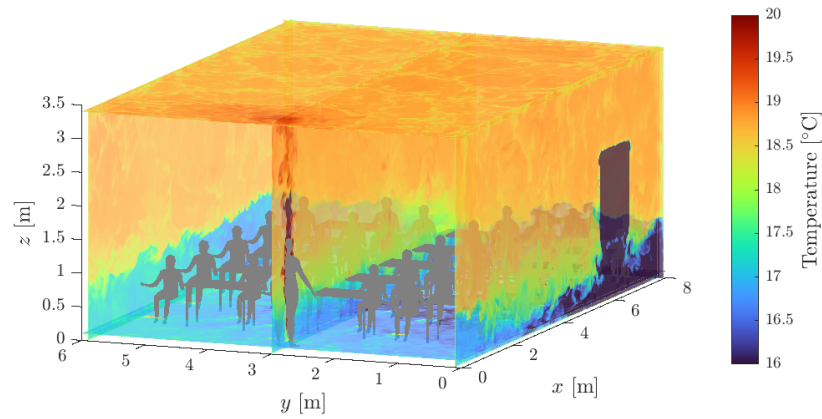


Figure 5: Instantaneous temperature field for case 1 after an hour.

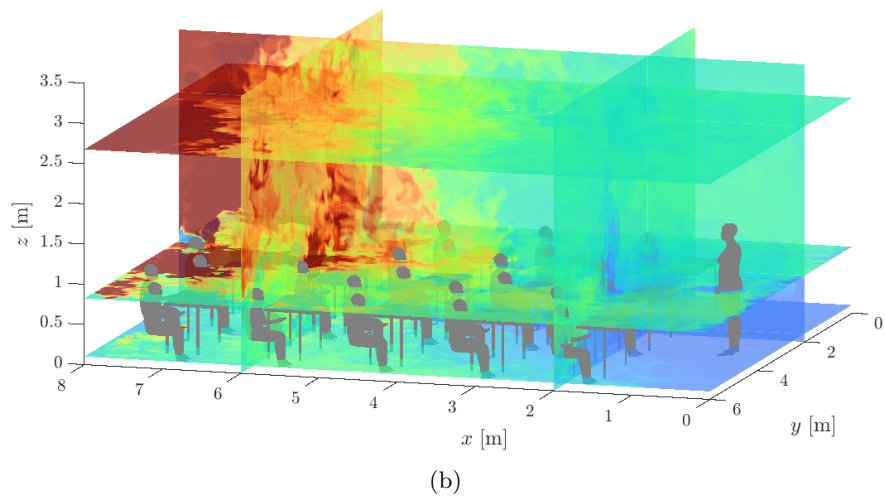
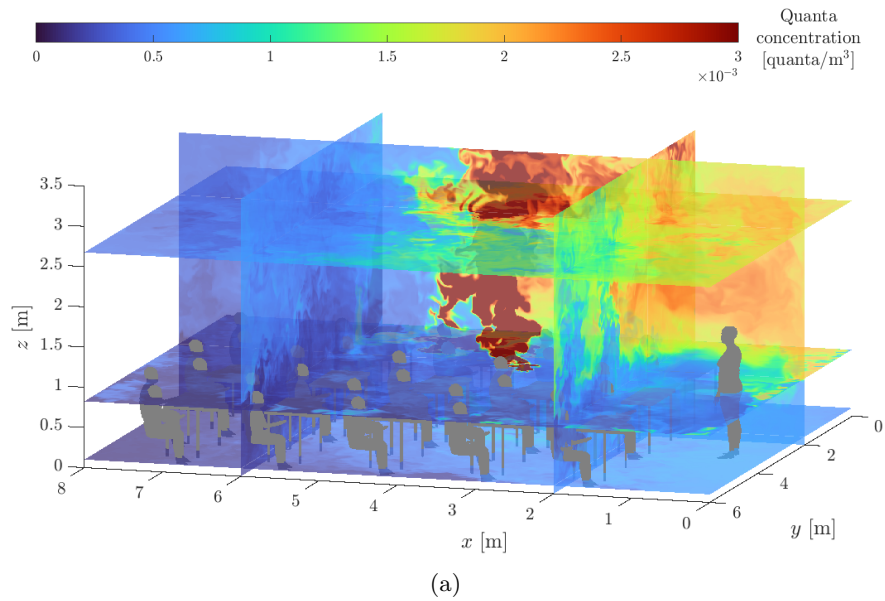


Figure 6: Instantaneous quanta concentration field slices for case 1, for the infected individuals sitting at (a) the front and (b) the back of the room.

3.1.2 Case 2: front window open

For the second simulation scenario, with the front window open, the results are shown in Figures 7, 8, 9 and 10.

The velocity field components depicted in Figure 7 show a similar behavior as the one observed for the first simulation case. Air enters the room at the open window, sinks due to thermal effects and a radial cold draft evolves from the impact point near the floor. On higher levels the airflow becomes more complex and is mainly driven by the thermal plumes and cooling at the walls.

Figure 8 show the mean flow at different heights. The cold draft near the floor exhibits a different pattern than the one observed for the first case. As the door is aligned with the open window, part of the cold draft moves directly towards the door and exits the domain. Nonetheless, another part moves towards the back of the room and progressively moves upwards due to thermal effects. On the other hand, upper levels' flow is once more dominated by thermal effects and many recirculations arise. A recirculation towards the open window also appears at mouth level for case 2.

For case 2, Figure 10 depicts the spatial tracer distribution. In the case of the infected child sitting at the front of the room, there are some noticeable differences with respect to case 1. In case 2, the pathogen is advected to the front of the room at breathing level (not backwards) due to the recirculation towards the open window, and upwards by the thermal plume. Nonetheless, less pathogen reaches the upper-front part of the classroom than in case 1. In contrast, part of the tracer is captured by the inflow air, reaches the floor and is then transported to breathing level. Consequently, case 2 allows for a more widespread and homogeneous tracer distribution at breathing level than case 1.

For the infected individual sitting at the back of the classroom, case 2 presents certain differences with case 1 due to the different upper level recirculations. Although in both cases the tracer travels mainly upwards, in case 2 a greater part of it is transported to the front of the room instead of moving to the back. This results in lower tracer concentrations at breathing and floor level in the student's area, but higher concentrations where the teacher is located.

3.1.3 General observations

Both cases show remarkable flow complexities, yet exhibit some common characteristics. In both cases the upper and lower room heights develop flows of different nature. Near the floor, cold drafts are induced by the inflow boundary condition and there is little recirculation. As progressively higher horizontal planes are inspected, the flow slows down and many recirculations arise, which are mostly directed towards the inflow boundary condition. Additionally, thermal effects become preponderant, with plumes forcing air upwards and descending drafts forming over the cold walls.

One of the main concerns for the simulated scenarios, apart from contagion risk, is thermal comfort. The child sitting next to the window will undoubtedly be colder, but the low cold draft generates a significant vertical temperature gradient for most occupants, which implies an adverse thermal comfort condition. Additionally, it is interesting to notice that children sit at the colder portion of the room. Therefore, the natural heating their thermal load provides is mainly wasted, as only the upper unoccupied portion of the room heats up.

Finally, the simulations confirm the existence of relevant pathogen concentration inhomogeneities at breathing level, which justify the need of evaluating to what extent Wells-Riley perfectly mixed models are valid.

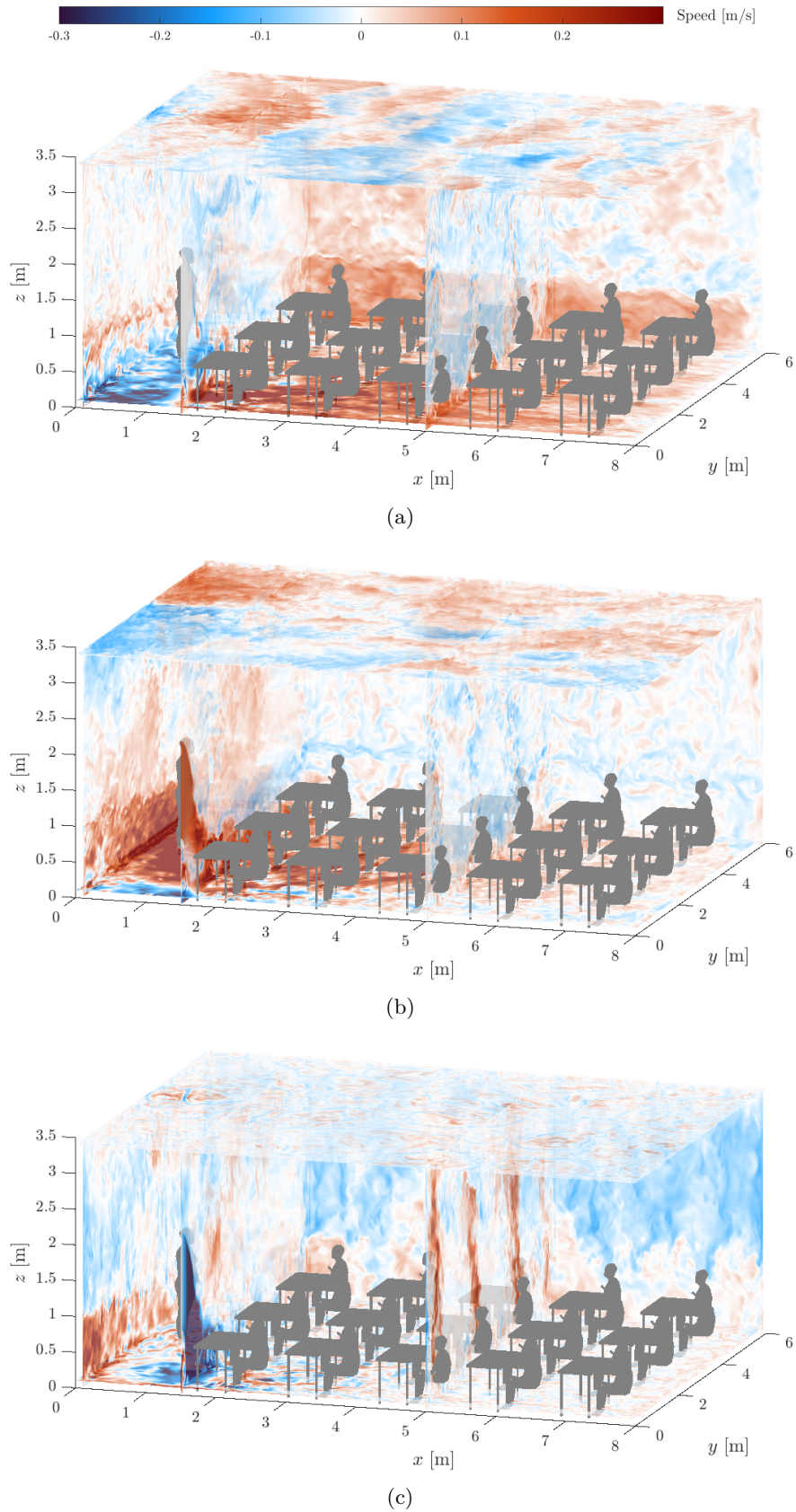
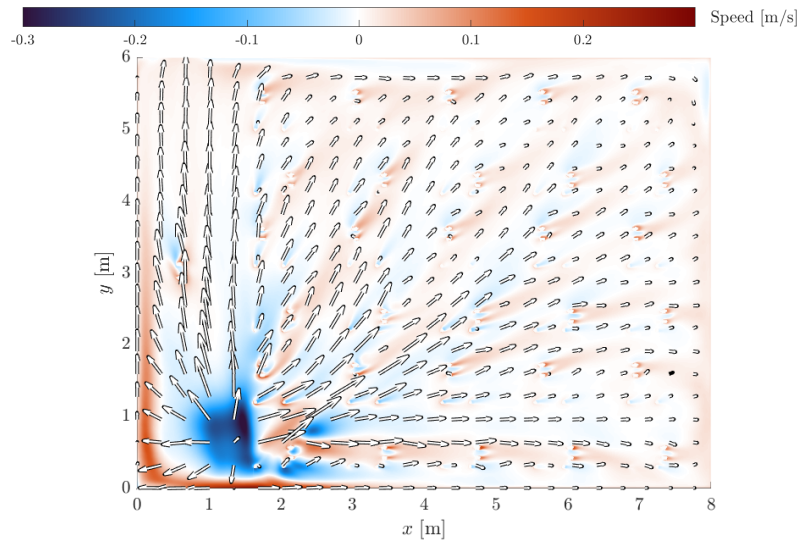
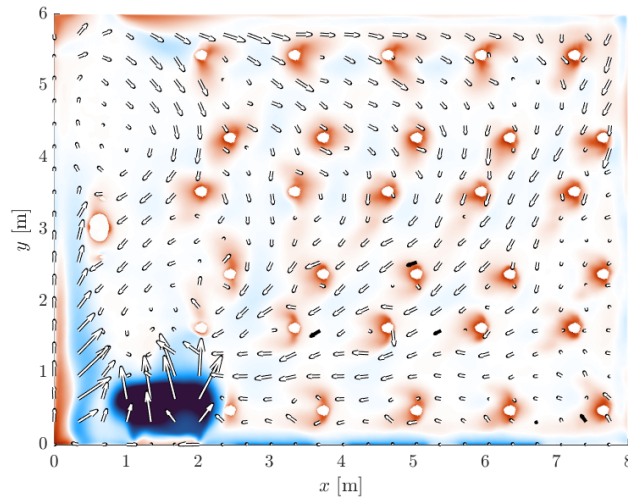


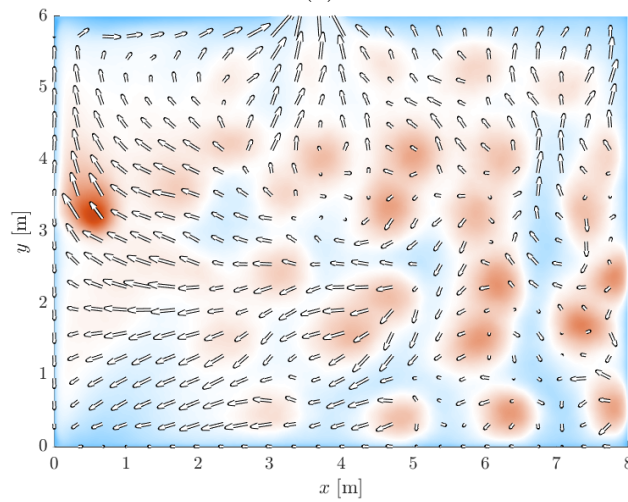
Figure 7: Velocity field slices for case 2. (a), (b) and (c) show the instantaneous velocity x , y and z components, respectively, after an hour of simulation.



(a)



(b)



(c)

Figure 8: Mean velocity field at different horizontal planes for case 2: (a) at 10 cm from the floor, (b) at the children's mouth level and (c) at the middle of the awning window. The coloured background corresponds to the vertical velocity component and the arrows show the horizontal projection of the velocity field.

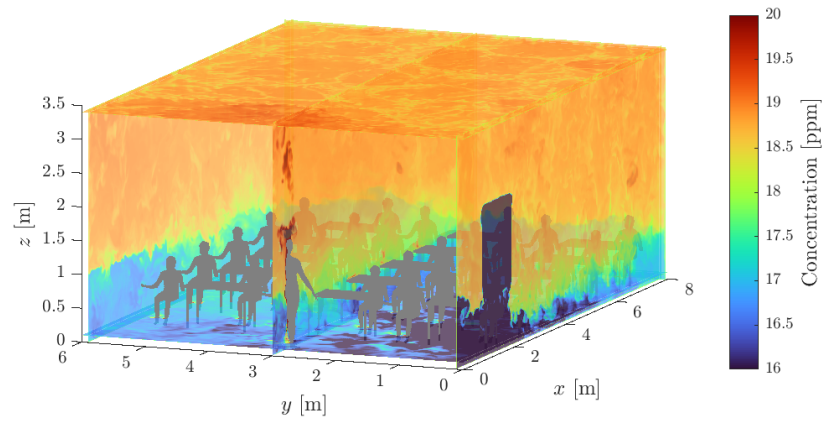


Figure 9: Instantaneous temperature field for case 2 after an hour.

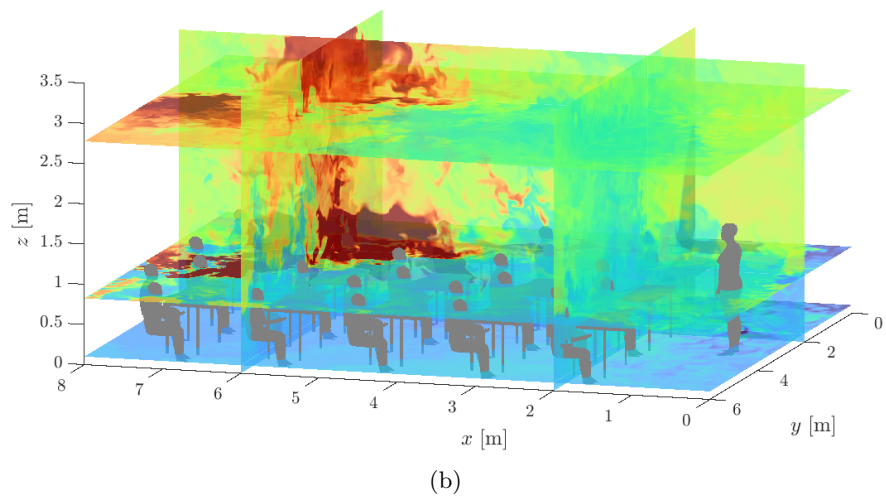
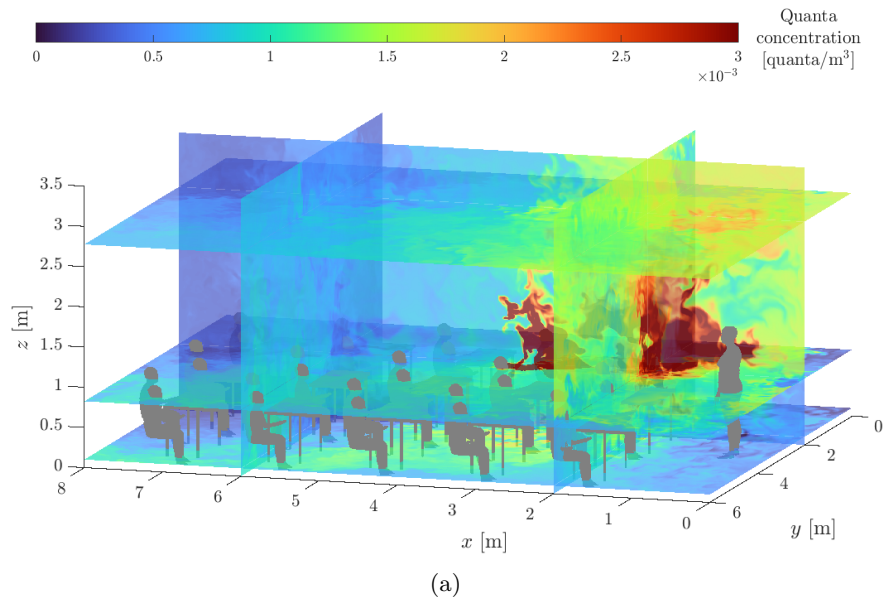


Figure 10: Instantaneous quanta concentration field slices for case 2, for the infected individuals sitting at (a) the front and (b) the back of the room.

3.2 Contagion risk at mouth level

3.2.1 Risk maps

For both simulation cases and for both infected children's positions, a risk map has been computed according to the described procedure in section 2.3. Risk has been evaluated for a one hour exposure period for both the first simulated hour (i.e. encompassing the initial transient flow) and the stationed concentration field. This aims at evaluating the importance of the transient process at the beginning of the simulation. The resulting maps were almost identical, meaning that the transient effects at the beginning of the simulation are not particularly relevant for the total risk. Therefore, only the steady state risk maps are reported.

The risk maps obtained for cases 1 and 2 are shown in Figures 11 and 12, respectively.

One of the most noticeable features in the results is that risk increases towards the open window, whether that is at the back (case 1) or at the front (case 2) of the room. This is associated with the recirculation patterns observed at mouth level, shown in Figures 4 and 8.

Furthermore, it is evident that there are important risk inhomogeneities for all scenarios. These are most important near the infected individual but, as the room is relatively crowded, higher risk zones comprise several other children in the room. At greater distances, spatial risk variations decrease.

Although the probability of infection might seem rather low (most commonly below 0.20%, and never above 1%), care should be taken when interpreting the absolute risk results. As it was previously mentioned, the analyzed scenario considers a quanta emission rate of 1 quanta/h. Nonetheless, quanta emission rates of more than 100 quanta/h have been suggested for SARS-CoV-2, and exposure events could last more than one hour. Consequently, risk values more than two orders of magnitude higher could be attained.

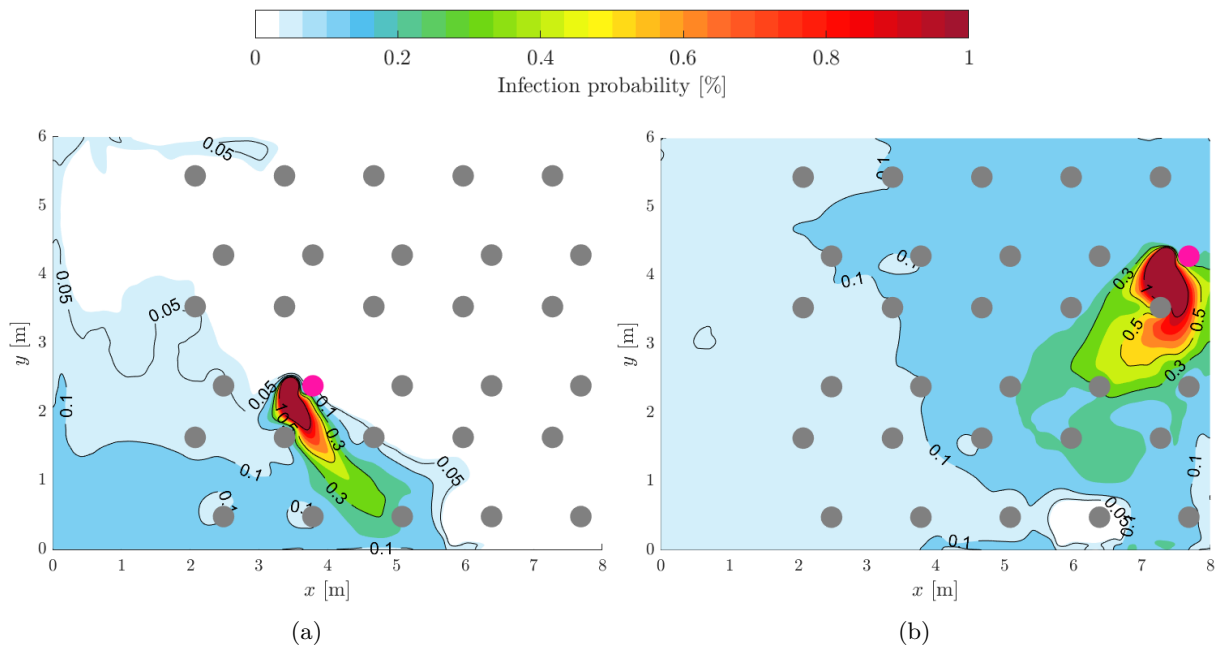


Figure 11: Risk maps for case 1 at children mouth level, considering a one hour steady state exposure with a quanta emission rate of 1 quanta/h. Grey circles represent the position of the head of susceptible children. The pink circle represents the infected individual, at either (a) the front or (b) the back of the classroom.

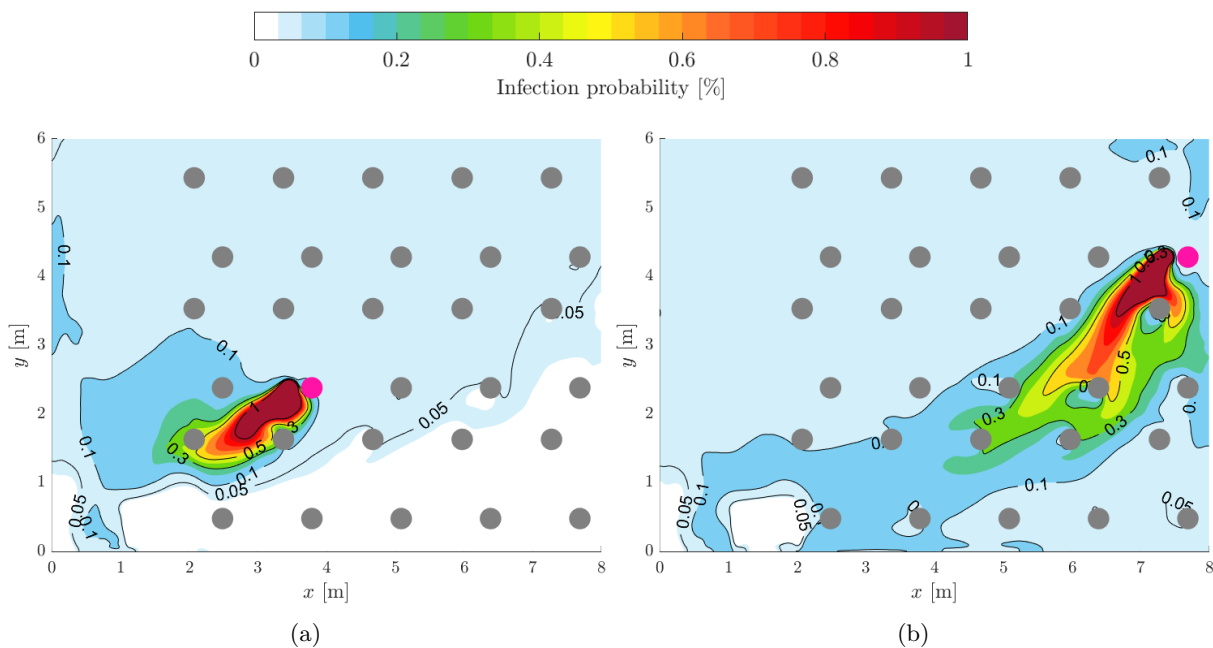


Figure 12: Risk maps for case 2 at children mouth level, considering a one hour steady state exposure with a quanta emission rate of 1 quanta/h. Grey circles represent the position of the head of susceptible children. The pink circle represents the infected individual, at either (a) the front or (b) the back of the classroom.

As it was previously mentioned, the presented risk maps can, up to a certain limit, be proportionally scaled for higher quanta emission rates and exposure times. This also allows for the inclusion of face masks, which can be represented by introducing a filtering factor in equation (6).

3.2.2 Comparison with the fully mixed Wells-Riley model

As we have restricted the results to the steady state portion of the CFD simulation, the equilibrium solution of equation (7) will be analyzed (i.e. the original Wells-Riley model). By setting the quanta time derivative to zero in equation (7), it can be shown [26] that in this case the predicted risk is given by equation (9).

$$P = 1 - e^{-\frac{PIqT}{Q}} \quad (9)$$

For the simulation conditions, the Wells-Riley box model results in an infection risk of 0.074%⁵. This is a reasonable estimation for some of the individuals (see lighter blue zones of the risk maps), but clearly underestimates the risk for many students. This is quantitatively evaluated in Figure 13, which shows the infection probability risk for each susceptible child as a function of the distance to the infected individual. Additionally, Figure 13 shows the fully mixed (and therefore independent of distance) analytical Wells-Riley model.

The highest risk was attained for case 1 with the infected individual sitting at the front, at the shortest distance. In this case, the risk predicted via the CFD coupled approach was approximately seven times higher than the one predicted via the traditional box model. Nonetheless, this was not the case for other configurations. Most noticeably, for case 1 with the infected individual at the back of the room, the highest risk was attained at a distance of more than 2 m, which is larger than the typical physical distancing recommendation for COVID-19 [23]. This is consistent with the results obtained in [9], and highlights the importance that flow inhomogeneities might play in indoors airborne infections.

Despite the fact that the fully mixed Wells-Riley model greatly underestimates the contagion risk at some positions, on average it has a relatively good performance. Even though the flow in the room was shown to

⁵For contrast, the transient Gammaitoni-Nucci model predicts a probability of 0.063%.

be extremely complex, the fully mixed model predicts a risk level that is appropriate for many occupants. Therefore, the model provides a simple and useful tool for mean risk assessment.

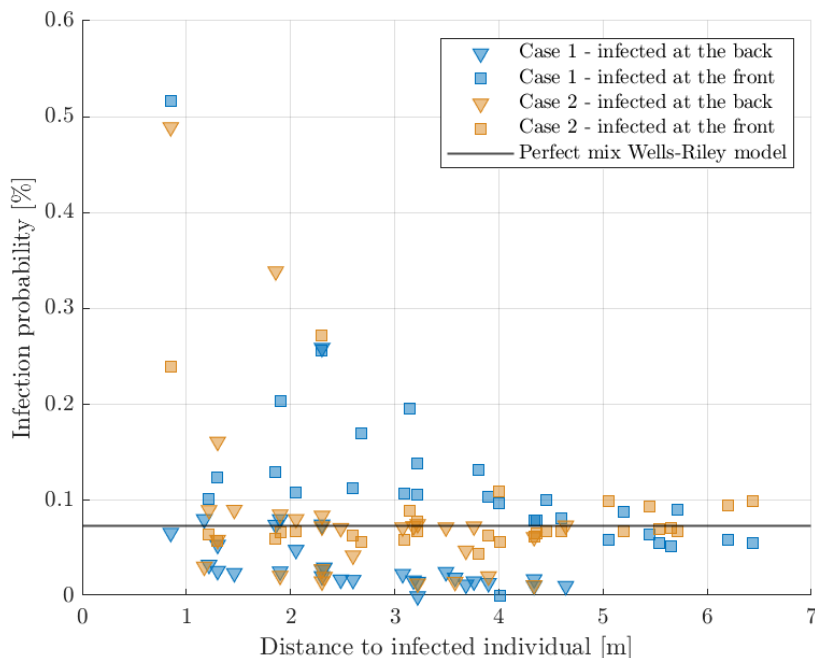


Figure 13: Infection probability as a function of distance to the infected individual obtained from the coupled CFD and Wells-Riley approach. The horizontal black line depicts the probability of infection estimated via the fully-mixed Wells-Riley approach.

4 Conclusions and future work

Highly resolved LES simulations of an indoor naturally ventilated school classroom during wintertime have been conducted. Airflow patterns were explored and passive tracers were used to assess the long distance airborne contagion risk of SARS-CoV-2 by coupling of the CFD results with a Wells-Riley approach. We particularly highlight the size and resolution of the CFD simulations, which attest to the great computational capabilities of CHAMAN.

The simulation results revealed remarkably complex airflow patterns. Thermal boundary conditions were found to be of the utmost importance, both at the inflow of cold air, which generated low cold drafts, and at the immersed boundaries of the occupants bodies, which generated thermal plumes that dominated the airflow from mouth height and above. The passive tracer fields further evidenced the flow complexities. In particular, recirculations towards the inflow boundary were observed at mouth level.

Additionally, the risk assessment methodology employed allowed for the generation of infection probability maps at mouth level. These suggest that pathogen inhomogeneities may play a significant role in airborne contagion, as local pathogen maxima significantly increase the probability of infection. Furthermore, the results showed that airborne contagion risk is mostly linked to airflow patterns and not to mere distance to the infected individual. Therefore, physical distancing could be insufficient to cope with long distance airborne infections.

The traditional fully mixed Wells-Riley approach was shown to provide an adequate estimation of the average risk of infection in the room, although it underestimates local risk maxima and overestimates risk for many positions. Despite this, given its simplicity, it remains a useful tool for quick risk assessment.

Further analysis of the preliminar simulation results is ongoing. In particular, grid independence and time convergence are being tested. Additionally, turbulence spectrum analysis will be performed.

Future work aims at simulation of more ventilation configurations, refinement of the initial and boundary conditions, validation via measurement campaigns and implementation of more physical models within

CHAMAN. In particular, we aim at implementing a Lagrangian particle module in order to evaluate the performance of the passive tracer approach. Additionally, the effects of virus inactivation and deposition could be explored, as well as the impact of not explicitly modelling the breathing of the occupants.

References

- [1] A. Cammarata and G. Cammarata. Dynamic assessment of the risk of airborne viral infection. *Indoor Air*, 31(6):1759–1775, 2021.
- [2] H. C. Burridge, R. K. Bhagat, M. E. J. Stettler, P. Kumar, I. De Mel, P. Demis, A. Hart, Y. Johnson-Llambias, M. F. King, O. Klymenko, A. McMillan, P. Morawiecki, T. Pennington, M. Short, D. Sykes, P. H. Trinh, S. K. Wilson, C. Wong, H. Wragg, M. S. Davies Wykes, C. Iddon, A. W. Woods, N. Mingotti, N. Bhamidipati, H. Woodward, C. Beggs, H. Davies, S. Fitzgerald, C. Pain, and P. F. Linden. The ventilation of buildings and other mitigating measures for COVID-19: A focus on wintertime. *Proceedings of the Royal Society A: Mathematical, Physical and Engineering Sciences*, 477(2247):20200855, 2021.
- [3] C. V. M. Vouriot, H. C. Burridge, C. J. Noakes, and P. F. Linden. Seasonal variation in airborne infection risk in schools due to changes in ventilation inferred from monitored carbon dioxide. *Indoor Air*, 31:1154–1163, 2021.
- [4] B. Pavilonis, A. M. Ierardi, L. Levine, F. Mirer, and E. A. Kelvin. Estimating aerosol transmission risk of SARS-CoV-2 in New York City public schools during reopening. *Environmental Research*, 195, 2021.
- [5] Z. Peng and J. L. Jimenez. Exhaled CO₂ as a COVID-19 infection risk proxy for different indoor environments and activities. *Environmental Science and Technology Letters*, 8:392–397, 2021.
- [6] L. Schibuola and C. Tambani. High energy efficiency ventilation to limit COVID-19 contagion in school environments. *Energy and Buildings*, 240:110882, 2021.
- [7] S. Peng, Q. Chen, and E. Liu. The role of computational fluid dynamics tools on investigation of pathogen transmission: Prevention and control. *Science of The Total Environment*, 746:142090, 2020.
- [8] M. Auvinen, J. Kuula, T. Grönholm, M.s Sühning, and A. Hellsten. High-resolution large-eddy simulation of indoor turbulence and its effect on airborne transmission of respiratory pathogens. Model validation and infection probability analysis. *Physics of Fluids*, 34(1):015124, 2022.
- [9] A. Foster and M. Kinzel. Estimating COVID-19 exposure in a classroom setting: A comparison between mathematical and numerical models. *Physics of Fluids*, 33(2):021904, 2021.
- [10] Z. Ai, C. M. Mak, N. Gao, and J. Niu. Tracer gas is a suitable surrogate of exhaled droplet nuclei for studying airborne transmission in the built environment. *Building Simulation*, 13:489–496, 2020.
- [11] P. Igounet, P. Alfaro, G. Usera, and P. Ezzatti. GPU Acceleration of the caffa3d.MB Model. In B. Murgante, O. Gervasi, S. Misra, N. Nedjah, A. M. Rocha, D. Taniar, and B. O. Apduhan, editors, *Computational Science and Its Applications – ICCSA 2012*, pages 530–542, Berlin, Heidelberg, 2012. Springer Berlin Heidelberg.
- [12] G. Fernandez, M. Mendina, and G. Usera. Heterogeneous Computing (CPU - GPU) for Pollution Dispersion in an Urban Environment. *Computation*, 8(1), 2020.
- [13] G. Usera, A. Vernet, and J. Ferre. A Parallel Block-Structured Finite Volume Method for Flows in Complex Geometry with Sliding Interfaces. *Flow, Turbulence and Combustion*, 81:471–495, 2008.
- [14] M. Mendina, M. Draper, A. P. Kelm Soares, G. Narancio, and G. Usera. A general purpose parallel block structured open source incompressible flow solver. *Cluster Computing*, 17:231–241, 2014.
- [15] J. Smagorinsky. General circulation experiments with the primitive equations. *Monthly Weather Review*, 91(3):99, 1963.
- [16] M. Draper, A. Guggeri, M. Mendina, G. Usera, and F. Campagnolo. A Large Eddy Simulation-Actuator Line Model framework to simulate a scaled wind energy facility and its application. *Journal of Wind Engineering and Industrial Aerodynamics*, 182:146–159, 2018.
- [17] M. Mendina and G. Usera. Numerical simulation of turbulent jet scour through implementation of a single phase eulerian model. *Journal of Irrigation and Drainage Engineering*, 148(2):04021069, 2022.
- [18] M. R. Pendar and J. C. Páscoa. Numerical modeling of the distribution of virus carrying saliva droplets during sneeze and cough. *Physics of Fluids*, 32, 8 2020.

- [19] M. Wang and Q. Chen. Assessment of various turbulence models for transitional flows in an enclosed environment (RP-1271). *HVAC&R Research*, 15:1099–1119, 2009.
- [20] G. K. Rencken, E. K. Rutherford, N. Ghanta, J. Kongoletos, and L. Glicksman. Patterns of SARS-CoV-2 aerosol spread in typical classrooms. *Building and Environment*, 204, 2021.
- [21] C. C. Liao, Y. W. Chang, C. A. Lin, and J. M. McDonough. Simulating flows with moving rigid boundary using immersed-boundary method. *Computers & Fluids*, 39(1):152–167, 2010.
- [22] University of Michigan Transportation Research Institute. BioHuman. [<http://humanshape.org/>], 2022.
- [23] WHO. Roadmap to improve and ensure good indoor ventilation in the context of COVID-19. Technical report, World Health Organization, 2021.
- [24] ASHRAE. ANSI/ASHRAE Standard 62.1-2019: Ventilation for Acceptable Indoor Air Quality. Standard 62.1 - 2019, American National Standards Institute, American Society of Heating and Refrigerating and Air-Conditioning Engineers, 2018.
- [25] W. F. Wells. *Airborne Contagion and Air Hygiene*. Harvard University Press, 1955.
- [26] E. C. Riley, G. Murphy, and R. L. Riley. Airborne Spread of Measles in a Suburban Elementary School. *American Journal of Epidemiology*, 107:421–432, 1978.
- [27] L. Gammaitoni and M. C. Nucci. Using a mathematical model to evaluate the efficacy of TB control measures. *Emerging Infectious Diseases*, 3:335–342, 1997.
- [28] L. Gammaitoni and M. C. Nucci. Using Maple to Analyze a Model for Airborne Contagion. *MapleTech*, 4:2–5, 11 1997.
- [29] S. N. Rudnick and D. K. Milton. Risk of indoor airborne infection transmission estimated from carbon dioxide concentration. *Indoor Air*, 13:237–245, 2003.
- [30] Y. Guo, H. Qian, Z. Sun, J. Cao, F. Liu, X. Luo, R. Ling, L. B. Weschler, J. Mo, and Y. Zhang. Assessing and controlling infection risk with Wells-Riley model and spatial flow impact factor (SFIF). *Sustainable Cities and Society*, 67:102719, 2021.
- [31] J. K. Gupta, C. H. Lin, and Q. Chen. Characterizing exhaled airflow from breathing and talking. *Indoor Air*, 20:31–39, 2010.
- [32] S. Fleming, M. Thompson, R. Stevens, C. Heneghan, A. Plüddemann, I. MacOnochie, L. Tarassenko, and D. Mant. Normal ranges of heart rate and respiratory rate in children from birth to 18 years of age: a systematic review of observational studies. *Lancet*, 377:1011–1018, 2011.
- [33] G. N. Sze To and C. Y. H. Chao. Review and comparison between the Wells-Riley and dose-response approaches to risk assessment of infectious respiratory diseases. *Indoor Air*, 20:2–16, 2 2010.
- [34] G. Buonanno, L. Morawska, and L. Stabile. Quantitative assessment of the risk of airborne transmission of SARS-CoV-2 infection: Prospective and retrospective applications. *Environment International*, 145, 12 2020.
- [35] G. Buonanno, L. Stabile, and L. Morawska. Estimation of airborne viral emission: Quanta emission rate of SARS-CoV-2 for infection risk assessment. *Environment International*, 141:105794, 8 2020.
- [36] Y. Wang, R. Chen, F. Hu, Y. Lan, Z. Yang, C. Zhan, J. Shi, X. Deng, M. Jiang, S. Zhong, B. Liao, K. Deng, J. Tang, L. Guo, M. Jiang, Q. Fan, M. Li, J. Liu, Y. Shi, X. Deng, X. Xiao, M. Kang, Y. Li, W. Guan, Y. Li, S. Li, F. Li, N. Zhong, and X. Tang. Transmission, viral kinetics and clinical characteristics of the emergent SARS-CoV-2 Delta VOC in Guangzhou, China. *EClinicalMedicine*, 40:101129, 10 2021.